Physicochemical properties of Pyr13TFSI-NaTFSI electrolyte for sodium batteries

Pierre Stigliano[a,b,c], Chiara Ferrara[a,], Nicolò Pianta[a], Antonio Gentile[a], Lorenzo Mezzomo[a], Roberto Lorenzi[a], Vittorio Berbenni[d], Riccardo Ruffo[a], Giovanni Battista Appetecchi[e], Piercarlo Mustarelli[a]*

a Department of Materials Science, University of Milano-Bicocca, Via Cozzi 55, 20215 Milano, Italy
b POLYMAT, University of the Basque Country UPV/EHU, Centro Joxe mari Korta, 20018, Donostia-San Sebastian, Spain
c Institute for Frontier Materials, Deakin University, Geelong, VIC 3220, Australia
d Department of Chemistry, University of Pavia, Viale Taramelli 16, 27100 Pavia, Italy
e ENEA, Materials and Physicochemical Processes Technical Unit (SSPT-PROMAS-MATPRO), Via Anguillarese 301, 00123, Rome, Italy
**Corresponding Author: Chiara Ferrara, chiara.ferrara@unimib.it*

Highlights

- The (1-x) Pyr13TFSI : x NaTFSI system was physico-chemically characterized over the entire solubility range.
- Electrochemical stability up to 4.5 V was demonstrated, allowing application of this ionic liquid as an electrolyte component for Sodium-Ion Batteries (SIBs).
- The composition x = 0.1 showed acceptable stability in a cell Na/IL/Na0.44MnO2.

Abstract

Ionic liquids (ILs) are an increasingly important component of electrolytes for lithium and sodium batteries. Here, the physicochemical properties of the system N-propyl-N-methylpyrrolidinium bis(trifluoromethanesulfonyl)imide ($Pyr_{13}TFSI$) ionic liquid and NaTFSI are investigated vs. the concentration of the sodium salt and the temperature. The explored concentration range was (1-*x*) $Pyr_{13}TFSI$: *x* NaTFSI with *x* (mole fraction) = 0, 0.02, 0.05, 0.1, 0.2. ^{23}Na solid-state NMR reveals that the Na^+ ions exist in two distinct environments: mobile Na^+ ions (1), and Na^+ ions involved in clusters or even bigger interacting networks (2). The ratio between mobile and bonded Na^+ populations increases with temperature and decreases with increasing salt concentration, reaching 100% at 60°C for the most diluted compositions. Raman spectroscopy allows to identify the quantity of free and bonded anions depending on the concentration, and to measure the number of Na^+ ions solvating the $TFSI^-$ anion (SN=4). The combined NMR and Raman results allow us to estimate the salt solubility range, $x = 0.12 \pm 0.02$. The composition $x = 0.1$ showed satisfying stability when cycled versus high-potential cathodic material $Na_{0.44}MnO_2$ (NMO) in a cell Na/IL/NMO.

Keywords: batteries, electrolyte, ionic liquid, structure, transport

Introduction

The development of safer and more performing electrolytes is a key step for the development of sodium-ion and sodium metal batteries. Indeed, the electrolyte covers a strategic role in determining the overall quality of the battery, as it not only represents the compartment responsible for the ionic conduction between the electrodes, but defines the operating potential window of the battery and determines its safety level through the formation of the Solid Electrolyte Interface (SEI) layer [1 - 4].

Sodium-ion battery electrolytes (both liquid and solid) are chiefly derived from the lithium-ion batteries technology, and are made of solutions of salts in mixtures of organic solvents [4], polymers [5, 6] or ionic liquids (ILs) [7, 8]. In particular, room temperature ionic liquids (RTILs) are constituted by combinations of salts whose eutectic point is below the room temperature itself. This peculiar feature is obtained thanks to weak coulombic interactions between the ions, which are generally due to the large size of the cation and to the delocalized charge on the anion. Both cation and anion structure can be modulated to tailor some specific properties, such as glass transition and melting temperature, viscosity, volatility [9]. The most common RTILs (simply ILs in the following) are based on imidazolium, pyrrolidinium, and quaternary ammonium salts as cations and bis(trifluoromethanesulphonyl)imide ($TFSI^-$), bis(fluorosulphonyl)imide (FSI^-), and hexafluorophosphate (PF_6^-) as the anions, with the use of NaFSI and/or NaTFSI as salts [8]. With respect to possible application as electrolyte components for rechargeable batteries, ILs are appealing because of their very low volatility and high flame-retardant properties, high electrochemical stability resulting in improved safety, good electrochemical performances, and environmental friendliness [3].

One of the major drawbacks of IL is their high viscosity, resulting in lower ionic conductivity than carbonate-based electrolytes [7-9]. Another crucial parameter is the Na^+ transference number, which is influenced by all the ionic species constituting the IL. While it is well established that the ionic conductivity of such systems is inversely related to the concentration [10-12], the electrochemical performances do not necessarily reflect this trend [13]. High overall conductivity values were reported for imidazolium, pyrrolidinium, and quaternary ammonium FSI salts in combination with NaFSI and NaTFSI, but this result did not always correspond to a high transference number for Na^+. This problem can be addressed by introducing more weakly coordinating anions, *e.g.,* by substituting FSI^- with $TFSI^-$ that should allow the cation to move more

freely. Due to the complex interplay among different parameters, *e.g*. anion and cation size, concentration, mixing of different species, etc., a careful investigation of the correlation among structure and properties of such systems is mandatory to determine the optimal composition in terms of viscosity, ionic transport, and operating voltage range.

In this work the physicochemical and functional properties of the binary electrolyte system based on the *N*-propyl-*N*-methylpyrrolidinium bis(trifluoromethanesulfonyl)imide ($Pyr_{13}TFSI$) ionic liquid and NaTFSI salt were systematically evaluated vs. the concentration of the sodium salt (from low concentration up to the solubility limit) and the temperature. The IL under study only contains the $TFSI^-$ anion, with the aim to weaken as much as possible the interactions with Na^+ and thus to increase the transference number. Moreover, the $TFSI^-$ based ILs was recently demonstrated to possess higher thermal stability in comparison with FSI^- analogues [14]. The physicochemical and structural properties obtained by the combined use of thermal analysis, electrochemical impedance spectroscopy (EIS), ^{23}Na solid-state NMR, and Raman spectroscopy were correlated with the electrochemical behavior of the IL in a cell $Na_{0.44}MnO_2$/IL/Na.

Experimental

Sample preparation – The pristine $Pyr_{13}TFSI$ (IL-PT) ionic liquid was synthesized and purified according to a procedure reported elsewhere [15][16], which allowed us to obtain materials with a halide and lithium content below 5 ppm, respectively. The NaTFSI (Solvionic, purity 99%) salt were used without any further purification and mixed with the proper amount of $Pyr_{13}TFSI$ to obtain different samples of the electrolyte system (1-*x*) $Pyr_{13}TFSI$: *x* NaTFSI with *x* = 0, 0.02, 0.05, 0.1, 0.2. Table 1 reports the labels for each sample and the relative compositions. For the x = 0.2 sample an undissolved amount of salt was obtained, independent of the heating/cooling cycles and/or

purification of the sample. After the preparation and before the analyses all the samples were purified with N_2 purging and distillation to eliminate the residual water. The final water content, as determined by Karl Fisher method, was below 5 ppm. All the samples were stored and handled in Ar-filled glove box (MBraun, O_2, H_2O < 0.1 ppm).

Thermal analysis - DSC Measurements were performed by a Heat Flux DSC apparatus Q2000 by TA Instruments (a Division of Waters Corporation, USA). The samples were weighed (in a glove box) in aluminum crucibles which were immediately sealed. The DSC cell was purged throughout the experiment with dry nitrogen flow of 50 mL/min. A sealed, empty aluminum pan was used as the reference. The thermal protocol consisted in: i) fast cooling down to -90°C (estimated average cooling rate 30°C/min); ii) rest at -90°C for 15' and, iii) heating at 10°C/min from the room temperature to 520°C. Thermogravimetric Analysis (TGA) was carried out using Mettler Toledo TGA/DSC-1, under argon atmosphere, heating at 10°C/min up to +100°C.

Raman spectroscopy - Micro-Raman measurements were performed at room temperature by a confocal LabRAM (Horiba Jobin-Yvon) spectrometer equipped with a He-Ne laser operating at 632.8 nm. The instrument operated in backscattering configuration, the scattered light was collected by a Long Working Distance 50x objective with a numerical aperture of 0.60 mounted on a microscope head (Olympus BX40) and detected by a charge coupled device (CCD-Sincerity, JobinYvon) with a resolution of 2 cm^{-1}. Raman spectra were acquired keeping the ionic liquids in sealed glass vials.

Solid-state NMR spectroscopy – ^{23}Na NMR spectra were acquired on a Bruker Avance III 9.4 T magnet equipped with a 4 mm Magic Angle Spinning (MAS) probe. The MAS rotors were filled with liquid samples in an Ar-filled glovebox (O_2, H_2O < 0.1 ppm). The NMR experiments were performed in static conditions (no rotors rotation). Both single pulse (256 scans, delay 2 s) and Inversion Recovery experiments (16 relaxation delays in the range 5 us - 1 s) were carried out in the

temperature range 25°- 60°C to obtain information on chemical shift, line broadening, and longitudinal relaxation time, T_1. The spectra were referenced to aqueous 0.1 M NaCl solution (0 ppm signal at room temperature) and analyzed with the use of TopSpin4.0™ (Bruker).

Conductivity – Ionic conductivity measurements were performed keeping the ionic liquid in sealed glass vials in the temperature range 10 - 100 °C using an Amel 192/K1 conductivity cell composed of two black platinum electrodes with a cell constant K = 1.06 cm^{-1}. To obtain the resistance of the ILs at different temperatures, Electrochemical Impedance Spectroscopy (EIS) analysis was performed in the frequency range 1 MHz-100 Hz with a signal amplitude of 10 mV.

Electrochemical measurements - The electrochemical stability window (ESW) of the ILs was tested by performing Cyclic Voltammetry (CV) at a scan rate of 1 mV s^{-1} in the voltage range 0.1-5.0 V vs. Na^+/Na on three-electrodes Swagelok-type cells employing carbon-coated aluminum as working, Na metal both as counter and reference electrode, and Celgard™ 2400 as separator. $Na_{0.44}MnO_2$ (NMO) slurries, applied on aluminum foil, were obtained by mixing 80 wt.% of active powder, 10 wt.% PVDF, and 10 wt.% Super-P carbon using *N*-Methyl-2-Pyrrolidone (NMP) as the solvent. The average loading of active material resulted in the order of 1 mg cm^{-2}. Galvanostatic Cycling with Potential Limitation (GCPL) tests were performed on CR2032-type coin cells employing Celgard™ 2400, metallic sodium and NMO as separators, negative and positive electrodes, respectively. Such analyses were carried out in the potential range 2.0-3.8 V vs. Na^+/Na at a current regime of C/10 (14.6 mA g^{-1}) both in charge and discharge. All the cells were sealed in an Ar-filled glove box (MBraun O_2, H_2O < 0.1 ppm) and tested using a VSP300 Biologic potentiostat/galvanostat.

Transference number – Sodium transference numbers were evaluated following the steady-state method [17]. Symmetric Na|electrolyte|Na cells were assembled for the three unsaturated compositions (0.02, 0.05 and 0.1). Then, a small potential difference (10 mV) was applied between the two electrodes and the current was recorded until a nearly constant value was reached. Two

impedance spectra, one collected before and the other after the chronoamperometry, were collected to obtain the charge transfer resistance of the system, and the transference number was obtained with the relationship:

$$t_{Na^+} = \frac{I_{s-s}}{I_p}\frac{V - I_p R_{i-tot}}{V - I_{s-s} R_{f-tot}} \qquad \text{(Equation 1)}$$

where I_{s-s} is the value of the current at the steady-state, I_p is the value of the current at the peak (corresponding to the formation of the double-layer at the electrodes), R_{i-tot} and R_{f-tot} are the total charge-transfer resistances before and after the chronoamperometry measurement, respectively.

[insert Table 1]

Results and discussion

The thermal behavior of the electrolytes was investigated in the temperature range -90°/+75°C. The results of the DSC investigation are reported in Figure 1 a,b. As expected, the DSC patterns are strongly dependent on the composition of the samples. Pure $Pyr_{13}TFSI$ (IL-PT) showed no glass transition and a clear melting endotherm peak at ~10 °C, in excellent agreement with the literature [18]. The addition of x = 0.02 of NaTFSI determined an enlargement of the melting endotherm and the decrease of T_m at ~5 °C. Further addition of NaTFSI caused a significant complication of the DSC thermograms, with the appearance of glass transitions (T_g), which will be discussed in detail in the following, of one or two cold crystallization phenomena in the range -60/-20°C, and of various melting peaks starting around ~0 °C. The presence of glass transitions and cold crystallization exotherms is due to amorphization of the samples during fast cooling. We stress that the DSC experiment is intrinsically performed out of equilibrium, and the actual amount of the amorphous phase(s) may also depend on the cooling rate. In the following, we will not focus on the amorphous/crystalline ratio, which is chiefly governed by kinetics issues. Concerning the

dependence from composition, we can state that the increased tendency of the system to undergo amorphization may be related to the increasing disorder introduced by the Na^+ cations, which have different dimensions and solvation power with respect to the Pyr_{13}^+ cations.

The presence of several endotherms is due to the presence of both *cis* and *trans* conformers of the $TFSI^-$ anion, which have different melting temperatures. If the sample is fully crystallized during cooling, $TFSI^-$ is only in the thermodynamically favoured *trans* form, and a single melting peak should be observed. In contrast, if the sample is partially amorphous, as in our case, both the forms are present, and two melting peaks are observed [19] [20].

According to previous results obtained for similar IL-based electrolytes [20], the presence of the salt is beneficial as it lowers the melting temperature of the electrolytes, thus expanding their operating temperature range. As expected, pure NaTFSI did not show any thermal feature in the investigated temperature range.

T_g were observed for the samples Na005, Na01, and Na-sat, at -83 °C, -80 °C, and -73 °C, respectively. Although in some cases the T_g starting point was near to the DSC stabilization temperature, we were able to correctly identify the glass transition. The T_g value increased with the salt concentration, as already observed for other Na-containing electrolytes Pyr_{13}FSI-NaTFSI [11], Pyr_{13}FSI-NaFSI [10], Pyr_{14}TFSI-NaTFSI [11, 12, 14, 21] and Li-containing systems [22 - 24]. The T_g increase was related to the formation of Li^+/Na^+ complexes/clusters with reduced mobility and, generally, to an increase in the strength of interactions among the system components [25]. As the formation of such complexes is affected by the charge/radius ratio and by the dimension of the involved ions, thus significant differences can be found between Li and Na-containing systems. Finally, the observed enthalpy endothermic overshoots can be related to a kinetic structural rearrangement in the viscous liquid state above the T_g [26].

Figure 1c shows the TGA behaviours of Na01 and Na-sat compositions i.e., the richest in salt content. The thermal stability is very high and exceeds 375 °C for both the compositions.

[insert Figure 1]

To get insight into the changes in the IL structure induced by the addition of NaTFSI, NMR and Raman spectra have been collected for all the samples. Figure 2a shows the ^{23}Na NMR spectra vs. temperature for all the samples. All the spectra present a single resonance centered at the –10 ppm. This resonance cannot be fitted properly with the use of a single contribution, but requires at least two Gaussian/Lorentzian components, called Peak 1 and Peak 2 in the following (Figure 2, dotted lines). Figures 2b-e report the results of the fitting procedure: (b) peak width at half maximum (FWHM), (c) chemical shift, (d) relative intensities of the two peaks, and the spin lattice relaxation time, T_1, of the overall spectrum (e). In fact, it was not possible to separate the contributions to the relaxation process provided by the two components. The existence of distinct Na populations with different mobility related to the different interaction strength with the environment was already reported for IL-based [27] and for polymer electrolytes [28] [29]. On the basis of previous literature [30] [31], Peak 1, at higher field, could be attributed to mobile Na^+ species, whereas Peak 2, at lower field, could be associated with Na^+ ions strongly interacting with the surrounding ions (*e.g.* forming clusters).

As a preliminary result, thanks to a careful control of the experimental parameters (delay time among NMR pulses, evaluation of the sample mass), as well as to the absence of quadrupolar satellite transitions, which make almost quantitative the evaluation of the peaks integrals, we were able to estimate the actual concentration of the Na-sat sample, where an undissolved fraction was present. We obtained $x \cong 0.11$ as the solubility limit, very near to the composition of Na01 sample, and in excellent agreement with the data obtained by Raman spectroscopy (see next Figure 3d and related discussion). Similar solubility limits were found in (EMITFSI-NaTFSI) [12] and

(Pyr$_{14}$TFSI-NaTFSI) [32] IL-based electrolytes. The analysis of the relevant NMR parameters reported in Figure 2b-e will thus be based on this starting point related to the actual composition.

[Insert Figure 2]

The NMR line broadening (Figure 2b) is inversely proportional to the spin-spin relaxation time, T_2, which in these systems is mainly influenced by atom mobility and site-exchange velocity [11]. The stronger the interaction the broader the peak, the higher the mobility the sharper the peak. Broader lines are thus associated with viscous or solid systems, while sharper lines are related to highly mobile species. Let's start to consider the NMR relaxation process. The T_1 values (Figure 2e) show a monotonous decrease vs. the temperature, which is more evident for the most concentrated compositions, Na005, Na01, and Na-sat. This means that these systems did not yet reach the motional narrowing minimum, $\omega\tau_c \approx 1$, where ω is the Larmor frequency and $\tau_c$is the correlation time for Na^+ ions motion. This is confirmed by comparing the T_1 values with the T_2 ones obtained by the relationship:

$$T_2 \cong \frac{1}{\pi \cdot FWHM} \qquad \text{(Equation 2)}$$

Because of the superposition principle of relaxation rates from different populations:

$$\frac{1}{T} = \sum_i \frac{p_i}{T_i} \qquad \text{(Equation 3)}$$

where $p_i$is the weight of the i-th population, it is possible to obtain the overall spin-spin relaxation rate $1/T_2$ including the contributions from peaks 1 and 2. To give an example, from the data of Figure 2b, at 25°C we obtained $T_2 \cong 95$ µs for Na005 and $T_2 \cong 66$ µs for Na-sat to be compared with $T_1 \cong 470$ µs and $T_1 \cong 510$ µs, respectively. At 60°C the values were $T_2 \cong 120$ µs for Na005 and $T_2 \cong 117$ µs for Na-sat to be compared with $T_1 \cong 390$ µs and $T_1 \cong 380$ µs, respectively.

In the motional narrowing regime, the relationship:

$$\left(\frac{1}{T_1}\right)_Q \cong \left(\frac{1}{T_2}\right)_Q \qquad \text{(Equation 4)}$$

holds for quadrupolar nuclei such as ^{23}Na, where the subscript "*Q*" refers to quadrupolar-driven relaxation mechanisms [33].

As a matter of fact, the T_1 and the T_2 values are well decoupled in all the explored temperature range, although, as expected, the difference is getting reduced by increasing the temperature. We can conclude that the system relaxation is still influenced by electric quadrupolar interaction [34], even at the highest temperature we examined.

Interestingly, the FWHM of the two components present different behaviors. Peak 1, attributed to more mobile Na^+ ions, and characterized by smaller values than Peak 2, chiefly at low temperature, shows a non-linear behavior with a maximum, which is particularly evident for the most diluted composition. Such a behavior was already reported for similar ILs [11, 25] and attributed to the interplay of two mechanisms: i) at low temperature, an exchange broadening, as the result of rapid site exchange detectable in the time scale of the NMR acquisition (of the order of milliseconds), ii) at high temperature, a decrease of the FWHM due to motional-induced line narrowing, with the increasing mobility of the ions averaging out all the interactions which lead to line broadening. However, these Authors discussed the NMR parameters for the overall ^{23}Na resonance without any distinction among different contributions. Peak 2, attributed to Na^+ ions strongly coupled with other IL moieties, shows a monotonous decrease vs. the temperature. This temperature dependence is indeed related to a change in the Na dynamics dominated by the electric quadrupolar interaction [25].

The ^{23}Na chemical shifts (Figure 2c) change as a function of both salt concentration and temperature. Globally, both the dependences are weak, as already reported for similar systems [35], and this is consistent with strong Na^+ - $TFSI^-$ interactions. In fact, according to the literature

[12], the Na^+ ions are coordinated by 6 oxygen atoms and the energetically preferred structure is $[Na(TFSI)_3]^{2-}$, indicating that $TFSI^-$ anions tend to chelate the Na cations. Interestingly, the chemical shifts of the two components show opposite behaviors with respect to FWHM. As expected, the component 1 (mobile Na^+ ions) has a monotonous shift downfield vs. temperature. In fact, the increasing temperature weakens the ionic interactions and therefore lessens the electron shielding effect from the anions. As a result, the cations become more positively charged and hence the chemical shift is less negative, i.e. it is moving towards the low-field (deshielded) region [11]. At a given temperature, more concentrated solutions show upfield shifts due to increased electron shielding of the cations. The component 2 (more bonded Na^+) shows a non-linear behavior vs. temperature, characterized by a maximum (in the downfield direction) around 35-40 °C for all the compositions. Again, this is due to the interplay of two competing effects. The initial downshift may be attributed to increasing Na^+ mobility. The maximum is likely reflecting a point where the average environment of the Na^+ ions is the same independent of concentration. The subsequent shift upfield at higher temperature could finally be due to fast anion exchange around Na^+ ions, causing increasing average shielding. We did not observe a dependence of the maximum from concentration, contrary to that reported by Yoon et al. on Pyr_{13}TFSI-NaFSI electrolytes [10].

Finally, the evaluation of the relative amount of components 1 and 2 (Figure 2d) indicates that, by increasing temperature, the clusters tend to dissociate (decrease of Peak 2), increasing the amount of mobile Na ions (increase of Peak 1). This behaviour is observed for all the compositions. However, for the less concentrated systems (Na002 and Na005) the number of clusters at high temperature is negligible, whereas the number of clusters and ionic couples for the most concentrated ones (Na01 and Na-sat) is still significant even at high temperature.

Summing up, overall information arising from the analysis of the NMR data reveals that the Na^+ ions are found in, at least, two distinct environments: population 1 associated with more mobile

Na^+ ions, and population 2 associated with Na^+ ions involved in clusters or strongly interacting networks. The two populations show different behavior with temperature, as the chemical shift and line broadening evolve differently. Further and complementary information, chiefly concerning the anions' solvation properties, is obtained by Raman spectroscopy.

Raman spectra of the full series of samples are shown in Figure 3a after baseline removal and normalization with respect to the main peak at 742 cm^{-1}. Spectra are the results of the superposition of signals from Pyr_{13}^+ cation and $TFSI^-$ anion. Pyr_{13}^+ characteristic signals are the symmetrical breathing mode of the pyrrolidine ring at 906 cm^{-1}, the CH_2 bending and deformation modes at 1041 cm^{-1} and 1460 cm^{-1}, respectively, and the superposition of alkyl stretching modes in the region 2800 - 3100 cm^{-1} [35]. The rest of the spectrum is related to $TFSI^-$ anion with a group of signals in the range 200 - 450 cm^{-1} with a stronger peak at 280 cm^{-1} from CF_3 rocking, and the others associated with SO_2 wagging, twisting, and rocking modes; three isolated peaks in the range 500 - 600 cm^{-1} from SO_2 and CF_3 bending modes; the most intense peak at 742 cm^{-1} which is a combination of SNS symmetric stretching and the CF_3 symmetric bending modes and reflects the contraction-expansion movement of the molecule; finally, the symmetric stretching modes of SO_2 and CF_3 are at 1140 cm^{-1} and 1245 cm^{-1}, respectively [36, 37].

After NaTFSI addition, the Raman spectra do not show any relevant modification, except variation in the relative intensities peak group in the region 200 - 450 cm^{-1} depending on relative population of *cis* and *trans* $TFSI^-$ conformers [38]. Indeed, significant insight about the system can be inferred by detailed analysis of the main peak at 742 cm^{-1}, as reported in Figure 3b. After normalization with respect to integrated peak intensities, the addition of NaTFSI seems to cause three main apparent effects: a peak shift toward higher wavenumbers, a lowering of peak height, and a peak broadening. This effect is caused by the presence of two different $TFSI^-$ moieties, namely, the free and the bound anions [37]. These two species feature very similar Raman signals shifted one from

the other by about 2 cm^{-1}. The free $TFSI^-$ is entirely solvated by the Pyr_{13}^+ cations, while the bound species interacts mainly with the Na^+ ions forming aggregates. This scenario is compatible with the NMR analysis. The amounts of bound anions can be detected only when the added salt is sufficient to cause a rearrangement of the structure of the ionic liquid, whereas in the pure IL-PT only the free $TFSI^-$ is present. In Figure 3c we report the peak decomposition analysis for pure IL-PT and for the sample with the highest concentration of Na (Na-sat). For IL-PT, only the free anion peak is present, whilst for Na-sat the band is fitted by the sum of two peaks corresponding to free and bound anions. The two peaks are both fitted by a pseudo-Voigt profile with identical FWHM of 8.2 cm^{-1} but centered at 741.9 cm^{-1} and 743.7 cm^{-1} for free and bound peak, respectively. Indeed, the two anions have similar vibrational responses and, more remarkably, they also have very similar Raman cross sections. Thus, the population of free and bound anions is proportional to the net area under the corresponding peak. Before studying the relative population, we need to carefully evaluate the effective concentration of the solutions, in particular of Na-sat, where we observed a precipitate indicating supersaturation. To measure the actual concentration of this solution, we used Raman spectroscopy as a quantitative tool. Figure 3d shows the Raman intensity of the breathing ring mode of pyrrolidine at 906 cm^{-1}, normalized with respect to the intensity of the $TFSI^-$ peak at 742 cm^{-1}, vs. the nominal concentration ratio $[TFSI^-]/[Pyr_{13}^+]$.

[Insert Figure 3]

Data show linear proportionality, within the experimental uncertainty, up to concentrations corresponding to the Na01 sample. As suggested from the presence of residue in the solution, for the nominal concentration $[TFSI^-]/[Pyr_{13}^+]=1.25$ the signal ratio is well below its expected value from trendline. Thus, the effective concentration can be inferred using the fitting line as a calibration curve and obtaining a true concentration value of $[TFSI^-]/[Pyr_{13}^+]=1.25$, which corresponds to an effective Na stoichiometric content x = 0.14, in good agreement with NMR

determination discussed above. Once the effective concentration has been established over the entire concentration range of the prepared solution, we can analyze the solvation mechanisms of the system. The solvation number (SN), representing the number of Na^+ ions solvating the $TFSI^-$ anion, can be calculated starting from the areas of the Raman bands relative to free (742 cm^{-1}) and bound TFSI (744 cm^{-1}) and assuming the same Raman cross-sections for the two transitions: $SN = I_{Bound} / (I_{Bound} + I_{Free}) = I_{744} / (I_{744} + I_{742})$ [12, 37, 38]. The results, reported in Figure 3e, show SN = 4 over the entire range of concentration, possibly lower for the highest Na concentration. This value is higher with respect to the Li solvation number in $Pyr_{13}TFSI$ solutions as a consequence of the reduced charge/radius ratio [12, 39].

Combining the insight on the Na and TFSI coordination obtained from NMR and Raman analysis it is possible to infer that the most favorable species is the $[Na(TFSI)_3]^{2-}$ involving SN = 3 and ionic aggregation. Indeed, the SN = 4 (as determined from Raman analysis) requires TFSI moieties acting both as bidentate and monodentate coordinating agents, involving the presence of different Na populations of solvated cations, ionic couples, and clusters. The $[Na(TFSI)_3]^{2-}$ species was already determined to be one of the most energetically favored in similar systems [12], supporting our hypothesis. An accurate determination of the species, relative population, and conformation of the Na-TFSI moieties present in the system can be obtained only through DFT calculations, as extensively demonstrated by previous work in this field [12, 30, 38].

[Insert Figure 4]

Figure 4 shows the Arrhenius plot of the ionic conductivity in the temperature range of interest for the possible application as electrolyte for SIBs. The pure IL shows the best values at every temperature, but for the lowest ones where incipient crystallization takes place determining a drop in conductivity, in agreement with the thermal results. The observed values are in good

agreement with the literature [9, 12]. As expected, the ionic conductivity decreases with the increase of the salt concentration; this effect has been associated to the increased viscosity of the systems [10-14, 40], in agreement with the increase of the population 2 of Na moieties involved in clusters and displaying reduced mobility as detected by NMR analysis. The conductivity values are in the same range previously reported for similar systems [13]. The conductivity of the Na02 sample presents the more significant dependence on temperature, while the Na002 the less pronounced one. In general, the dependence of conductivity on temperature increases with the salt concentration, as already observed for the Pyr_{13}FSI-NaFSI [12] and Pyr_{14}TFSI-NaTFSI [40] systems. The dependence of the conductivity, σ, vs. temperature can be modeled in terms of the empirical Vogel-Tammann-Fulcher (VTF) relationship:

$$\sigma = \sigma_0 exp\left[\frac{-B}{(T-T_0)}\right] \qquad \text{(Equation 3)}$$

where the pre-exponential parameter, σ_0, is related to the number of charge carriers in the electrolyte; B is referred to as the pseudo-activation energy for ion transport; and T_0 can be considered as the temperature at which the free volume disappears, or the configurational entropy in the electrolyte approaches zero [41]. The results of the VTF best-fits are reported in Table 2. The best-fitted parameters don't show any clear trend. However, the T_0 parameters are in good agreement with the experimental T_g, when observed.

[Insert Table 2]

To get further insight in the transport properties of the system, the transference numbers were evaluated using the Evans-Bruce-Vincent method [42]. Figure 5 shows the pertinent chronoamperometry data. We obtained t_{Na^+}= 0.40, 0.48, and 0.20 for Na002, Na005 and Na01, respectively. We could not perform a reliable measurement of Na-sat, because of the presence of a solid residue. We highlight the obtained values could be affected by significant errors because of

the high ratio between the interfacial and the bulk resistances obtained by EIS measurements (see Figure 5) [15]. Therefore, we will consider them only as far their trend is concerned, rather than rely on their absolute values. There is a non-monotonic growing trend of t_{Na^+} with the concentration, which calls again for the interplay between increase of sodium concentration, ion-ion association and increase of viscosity [17], although also the complex structure of clusters and interactions network evidenced by Raman and NMR analyses must be considered. Similar non-linear behaviours were obtained by Nicotera et al. by means on Pulse Field Gradient (PFG) NMR on the similar system Pyr_{13}TFSI-LiTFSI, and attributed to different degrees of ionic association. [43] We also stress that the change in the interfacial impedance before and after polarization is large, which can increase the uncertainty on transference number determination. This may be due to the instability of Na surface with time. We performed some sensitivity tests which showed that, in any case, the related kinetics is slow.

[Insert Figure 5]

The electrochemical stability was then evaluated with CV at a scan rate of 1 mv s^{-1} to state their possible use into working devices based on performing high-potential positive electrodes. To simulate a more realistic condition of compatibility with different cathodic materials, carbon-coated aluminum was used as WE, whereas CE and RE were both made of Na metal. As clearly visible in Figure 6, all the samples showed high current above 3 V during the first cycle, with the presence of peaks around 3, 3.5, and 4.5 V. These can be related to the formation of a stable interphase and/or to corrosion of the stainless steel (AISI304) parts of the Swagelok cell which can eventually meet the electrolyte. Indeed, the current then reduced during the next cycles until it reached stable values in very few cycles. As visible in Figure 6, no significant current flow at potential below 4.2 V vs. Na^+/Na was observed after 5 cycles for the Na002, Na005, and Na01 samples, demonstrating the stability of the electrolytes. The electrochemical stability increased by

increasing the salt content. This can be rationalized by considering that stability window in this ILs family is chiefly determined by anion oxidation. [16] The addition of salt causes the increase of ion-ion interactions with respect to the pure liquid, because of the Na^+ smaller ionic radius with respect to Pyr_{13}^+. This, in turn, determines the increase of the $TFSI^-$ stability vs. oxidation, as already observed for Li-based ILs. [40] The best results were provided by Na01. In contrast, for the Na-sat composition the current density was not negligible, probably due to residue of undissolved salts in the system. For this reason, we did not consider this last composition for further characterization.

[Insert Figure 6]

After having verified their stability in a wide electrochemical window, the IL-based electrolytes were finally tested via GCPL in coin cells employing NMO as the cathodic active material and Na as the anode. The best results in terms of cycling stability were achieved by the Na01 sample. Noteworthy, the compositions Na002 and Na005, which had higher conductivity and transference number, showed a faster degradation during cell cycling. This was likely due to a worse passivation layer formed during the first cycles. We infer that the highest stability upon cycling of the most concentrated solution can be explained considering the previously reported concepts of *solvent-in-salt* electrolytes [44]. Deeper studies are needed to address this point. As shown in Figure 7a,b, the cell based on the Na01 composition was able to operate stably for more than 20 cycles at C/10, delivering discharge capacities higher than 60 mA h g^{-1} with coulombic efficiencies in the range 90-95%. The relatively low values of coulombic efficiency are in line with what was obtained for systems employing NMO [45] or similar ionic liquids [32] in the absence of additives that can stabilize the interface between the cathode material and the electrolyte.

Overall, such tests confirmed the satisfying stability of our ILs even when cycled versus high-potential cathodic materials and metallic sodium. We finally stress that the increase in capacity observed after the first cycle was due to system stabilization. In particular, the electrolyte needs some time to optimally wet the electrode. This was observed in several other systems. [46-48]

[Insert Figure 7]

Conclusions

In this paper we investigated the physico-chemical and the structural properties, and the electrochemical performances of the electrolyte system (1-*x*) Pyr_{13}TFSI : *x* NaTFSI, by exploring the full solubility range of the NaTFSI in IL-PT. The maximum solubility was quantified with the combined use of NMR and Raman analysis, converging in determining $x = 0.12 \pm 0.02$. All the samples presented electrochemical stability, higher than 4.2 V, after a few stabilization cycles where impurity oxidation and SEI formation was observed. This makes them possible candidates as electrolytes in SIBs with high-voltage cathode materials. The electrochemical tests in half cell configuration using NMO as the cathode material showed that the Na01 sample can provide the best performance in terms of stability and delivered specific capacity. In the Na01 sample, indeed, the larger ion concentration decreases the interfacial electrode resistance, as also proved for the symmetric Na/(1-*x*) Pyr_{13}TFSI : *x* NaTFSI/Na cells (see insets of Figure 5). This promising electrochemical behavior is associated with a favorable combination of structural/transport features, provided that the Na01 sample showed worse transport properties with respect to more diluted compositions. This, in turn, can be ascribed to the good SEI-forming properties of concentrated solutions. While this effect is known, the specific structural and dynamical features that contribute to determine the global electrochemical stability do require further experimental/theoretical investigation.

Acknowledgements

Funding by the Italian Ministry of University and Research (MIUR) through grant “Dipartimenti di Eccellenza - 2017 “Materials for Energy”.

Funding by the Italian Ministry of Foreign Affairs and International Cooperation, in the frame of bilateral Italy-Israel ENVIRONMENTALIST project, is gratefully acknowledged.

Funding by the Italian Ministry of University and Research (MUR) in the frame of the PRIN project 2017MCEEY4, TRUST (Towards sustainable, high-performing, all-solid-state sodium-ion batteries), is gratefully acknowledged.

References

[1] A. Boschin, Sodium Batteries: From Liquid to Polymer Electrolytes, 2016.

[2] Q. Pan, D. Gong, Y. Tang, Recent progress and perspective on electrolytes for sodium/potassium-based devices, Energy Storage Mater. 31 (2020) 328–343. https://doi.org/10.1016/j.ensm.2020.06.025.

[3] G.G. Eshetu, G.A. Elia, M. Armand, M. Forsyth, S. Komaba, T. Rojo, S. Passerini, Electrolytes and Interphases in Sodium-Based Rechargeable Batteries: Recent Advances and Perspectives, Adv. Energy Mater. 10 (2020). https://doi.org/10.1002/aenm.202000093.

[4] Y. Sun, P. Shi, J. Chen, Q. Wu, X. Liang, X. Rui, H. Xiang, Y. Yu, Development and challenge of advanced nonaqueous sodium ion batteries, EnergyChem. 2 (2020) 100031. https://doi.org/10.1016/j.enchem.2020.100031.

[5] H. Yin, C. Han, Q. Liu, F. Wu, F. Zhang, Y. Tang, Recent Advances and Perspectives on the Polymer Electrolytes for Sodium/Potassium-Ion Batteries, Small. 17 (2021) 1–23. https://doi.org/10.1002/smll.202006627.

[6] F. Xu, S. Deng, Q. Guo, D. Zhou, X. Yao, Quasi-Ionic Liquid Enabling Single-Phase Poly(vinylidene fluoride)-Based Polymer Electrolytes for Solid-State $LiNi_{0.6}Co_{0.2}Mn_{0.2}O_2||Li$ Batteries with Rigid-Flexible Coupling Interphase, Small Methods, 5 (2021) 2100262 https://doi.org/10.1002/smtd.202100262.

[7] W. Zhou, M. Zhang, X. Kong, W. Huang, Q. Zhang, Recent Advance in Ionic-Liquid-Based Electrolytes for Rechargeable Metal-Ion Batteries, Adv. Sci. 8 (2021) 1–21. https://doi.org/10.1002/advs.202004490.

[8] M. Armand, F. Endres, D.R. MacFarlane, H. Ohno, B. Scrosati, Ionic-liquid materials for the electrochemical challenges of the future, Nat. Mater. 8 (2009) 621–629. https://doi.org/10.1038/nmat2448.

[9] M. Galiński, A. Lewandowski, I. Stepniak, Ionic liquids as electrolytes, Electrochim. Acta. 51 (2006) 5567–5580. https://doi.org/10.1016/j.electacta.2006.03.016.

[10] K. Matsumoto, Y. Okamoto, T. Nohira, R. Hagiwara, Thermal and transport properties of Na[N(SO2F)2]-[N -Methyl- N -propylpyrrolidinium][N(SO2F)2] ionic liquids for Na secondary batteries, J. Phys. Chem. C. 119 (2015) 7648–7655. https://doi.org/10.1021/acs.jpcc.5b01373.

[11] H. Yoon, H. Zhu, A. Hervault, M. Armand, D.R. MacFarlane, M. Forsyth, Physicochemical properties of N-propyl-N-methylpyrrolidinium bis(fluorosulfonyl)imide for sodium metal battery applications, Phys. Chem. Chem. Phys. 16 (2014) 12350–12355. https://doi.org/10.1039/c4cp00365a.

[12] D. Monti, E. Jónsson, M.R. Palacín, P. Johansson, Ionic liquid based electrolytes for sodium-ion batteries: Na+ solvation and ionic conductivity, J. Power Sources. 245 (2014) 630–636. https://doi.org/10.1016/j.jpowsour.2013.06.153.

[13] C. Ding, T. Nohira, R. Hagiwara, K. Matsumoto, Y. Okamoto, A. Fukunaga, S. Sakai, K. Nitta, S. Inazawa, Na[FSA]-[C3C1pyrr][FSA] ionic liquids as electrolytes for sodium secondary batteries: Effects of Na ion concentration and operation temperature, J. Power Sources. 269 (2014) 124–128. https://doi.org/10.1016/j.jpowsour.2014.06.033.

[14] L.G. Chagas, S. Jeong, I. Hasa, S. Passerini, Ionic Liquid-Based Electrolytes for Sodium-Ion Batteries: Tuning Properties to Enhance the Electrochemical Performance of Manganese-Based Layered Oxide Cathode, ACS Appl. Mater. Interfaces. 11 (2019) 22278–22289. https://doi.org/10.1021/acsami.9b03813.

[15] M. De Francesco, E. Simonetti, G. Gorgi, G. Appetecchi, About the Purification Route of Ionic Liquid Precursors, Challenges. 8 (2017) 11. https://doi.org/10.3390/challe8010011.

[16] M. Montanino, F. Alessandrini, S. Passerini, G.B. Appetecchi, Water-based synthesis of hydrophobic ionic liquids for high-energy electrochemical devices, Electrochim. Acta. 96 (2013) 124–133. https://doi.org/10.1016/j.electacta.2013.02.082.

[17] E. Tarlton, A. McKay, Canadian Journal of Chemistry, Amino Acids. 36 (1958) 496–506.

[18] M. Kunze, S. Jeong, E. Paillard, M. Winter, S. Passerini, Melting behavior of pyrrolidinium-based ionic liquids and their binary mixtures, J. Phys. Chem. C. 114 (2010) 12364–12369. https://doi.org/10.1021/jp103746k.

[19] W.A. Henderson, S. Passerini, Phase behavior of ionic liquid-LiX mixtures: Pyrrolidinium cations and TFSI- anions, Chem. Mater. 16 (2004) 2881–2885.

https://doi.org/10.1021/cm049942j.

[20] J. Serra Moreno, G. Maresca, S. Panero, B. Scrosati, G.B. Appetecchi, Sodium-conducting ionic liquid-based electrolytes, Electrochem. Commun. 43 (2014) 1–4. https://doi.org/10.1016/j.elecom.2014.02.010.

[21] S.A. Mohd Noor, P.C. Howlett, D.R. Macfarlane, M. Forsyth, Properties of sodium-based ionic liquid electrolytes for sodium secondary battery applications, Electrochim. Acta. 114 (2013) 766–771. https://doi.org/10.1016/j.electacta.2013.09.115.

[22] A. Martinelli, A. Matic, P. Jacobsson, L. Börjesson, A. Fernicola, B. Scrosati, Phase behavior and ionic conductivity in lithium bis(trifluoromethanesulfonyl)imide-doped ionic liquids of the pyrrolidinium cation and bis(trifluoromethanesulfonyl)imide anion, J. Phys. Chem. B. 113 (2009) 11247–11251. https://doi.org/10.1021/jp905783t.

[23] K. Ito, N. Nishina, H. Ohno, Enhanced ion conduction in imidazolium-type molten salts, Electrochim. Acta. 45 (2000) 1295–1298. https://doi.org/10.1016/S0013-4686(99)00335-7.

[24] M.J. Monteiro, F.F.C. Bazito, L.J.A. Siqueira, M.C.C. Ribeiro, R.M. Torresi, Transport coefficients, Raman spectroscopy, and computer simulation of lithium salt solutions in an ionic liquid, J. Phys. Chem. B. 112 (2008) 2102–2109. https://doi.org/10.1021/jp077026y.

[25] M. Hilder, M. Gras, C.R. Pope, M. Kar, D.R. Macfarlane, M. Forsyth, L.A. O'Dell, Effect of mixed anions on the physicochemical properties of a sodium containing alkoxyammonium ionic liquid electrolyte, Phys. Chem. Chem. Phys. 19 (2017) 17461–17468. https://doi.org/10.1039/c7cp03318d.

[26] P. Mustarelli, C. Tomasi, M. Villa, Heat capacities of thermally treated Na2O-3B2O3 glasses above and below Tg, Zeitschrift Fur Naturforsch. - Sect. A J. Phys. Sci. 51 (1996) 187–191.

https://doi.org/10.1515/zna-1996-0309.

[27] C.R. Pope, K. Romanenko, D.R. MacFarlane, M. Forsyth, L.A. O'Dell, Sodium ion dynamics in a sulfonate based ionomer system studied by 23Na solid-state nuclear magnetic resonance and impedance spectroscopy, Electrochim. Acta. 175 (2015) 62–67. https://doi.org/10.1016/j.electacta.2015.03.131.

[28] K.J. Adamić, S.G. Greenbaum, M.C. Wintersgill, J.J. Fontanella, Ionic conductivity in solid, crosslinked dimethylsiloxane-ethylene oxide copolymer networks containing sodium, J. Appl. Phys. 60 (1986) 1342–1345. https://doi.org/10.1063/1.337307.

[29] Y.S. Pak, K.J. Adamic, S.G. Greenbaum, M.C. Wintersgill, J.J. Fontanella, C.S. Coughlin, Complex impedance and multifrequency 23Na NMR study of poly (propylene oxide) complexed with NaB(C6H5)4, Solid State Ionics. 45 (1991) 277–284. https://doi.org/10.1016/0167-2738(91)90162-5.

[30] P. Geysens, V.S. Rangasamy, S. Thayumanasundaram, K. Robeyns, L. Van Meervelt, J.P. Locquet, J. Fransaer, K. Binnemans, Solvation Structure of Sodium Bis(fluorosulfonyl)imide-Glyme Solvate Ionic Liquids and Its Influence on Cycling of Na-MNC Cathodes, J. Phys. Chem. B. 122 (2018) 275–289. https://doi.org/10.1021/acs.jpcb.7b10158.

[31] R.H. Erlich, A.I. Popov, Spectroscopic Studies of Ionic Solvation. X. a Study of the Solvation of Sodium Ions in Nonaqueous Solvents by 23Na Nuclear Magnetic Resonance, J. Am. Chem. Soc. 93 (1971) 5620–5623. https://doi.org/10.1021/ja00751a005.

[32] I. Hasa, S. Passerini, J. Hassoun, Characteristics of an ionic liquid electrolyte for sodium-ion batteries, J. Power Sources. 303 (2016) 203–207. https://doi.org/10.1016/j.jpowsour.2015.10.100.

[33] I. Ruggeri, A. La Monaca, F. De Giorgio, F. Soavi, C. Arbizzani, V. Berbenni, C. Ferrara, P. Mustarelli, Correlating Structure and Properties of Super-Concentrated Electrolyte Solutions: ^{17}O NMR and Electrochemical Characterization, ChemElectroChem. 6 (2019) 4002–4009. https://doi.org/10.1002/celc.201900829.

[34] A. Abragam, The Principles of Nuclear Magnetism, 1961, Oxford University Press: London.

[35] I. Rey, P. Johansson, J. Lindgren, J.C. Lasse, Spectroscopic and Theoretical Study of $(CF_3SO_2)_2N$(TFSI) and $(CF_3SO_2)_2NH$(HTFSI), J. Phys. Chem. A. 102 (1998) 3249–3258.

[36] V.H. Paschoal, L.F.O. Faria, M.C.C. Ribeiro, Vibrational Spectroscopy of Ionic Liquids, Chem. Rev. 117 (2017) 7053–7112. https://doi.org/10.1021/acs.chemrev.6b00461.

[37] G.A. Giffin, N. Laszczynski, S. Jeong, S. Jeremias, S. Passerini, Conformations and vibrational assignments of the (fluorosulfonyl) (trifluoromethanesulfonyl)imide anion in ionic liquids, J. Phys. Chem. C. 117 (2013) 24206–24212. https://doi.org/10.1021/jp408565b.

[38] J.C. Lassègues, J. Grondin, D. Talaga, Lithium solvation in bis(trifluoromethanesulfonyl)imide-based ionic liquids, Phys. Chem. Chem. Phys. (2006) 5629–5632. https://doi.org/10.1039/b615127b.

[39] Y. Umebayashi, T. Yamaguchi, S. Fukuda, T. Mitsugi, M. Takeuchi, K. Fujii, S.I. Ishiguro, Raman spectroscopic study on alkaline metal ion solvation in 1-butyl-3-methylimidazolium bis(trifluoromethanesulfonyl)amide ionic liquid, Anal. Sci. 24 (2008) 1297–1304. https://doi.org/10.2116/analsci.24.1297.

[40] S. Brutti, M.A. Navarra, G. Maresca, S. Panero, J. Manzi, E. Simonetti, G.B. Appetecchi, Ionic liquid electrolytes for room temperature sodium battery systems, Electrochim. Acta. 306 (2019) 317–326. https://doi.org/10.1016/j.electacta.2019.03.139.

[41] C. A. Angell, Y. Ansari, Z. Zhao, Ionic Liquids: Past, present and future, Faraday Discussions (2012) 154, pp. 9-27. https://doi.org/10.1039/c1fd00112d.

[42] J. Evans, C.A. Vincent, P.G. Bruce, Electrochemical measurement of transference numbers in polymer electrolytes, Polymer 28 (1987) 2324-2328. https://doi.org/10.1016/0032-3861(87)90394-6

[43] I. Nicotera, C. Oliviero, W.A. Henderson, G.B. Appetecchi, S. Passerini, NMR Investigation of Ionic Liquid−LiX Mixtures: Pyrrolidinium Cations and TFSI- Anions; J. Phys. Chem. B, 2005, 109 (48), 22814-22819• DOI: 10.1021/jp053799

[44] L. Suo, Y.S. Hu, H. Li, M. Armand, L. Chen, A new class of Solvent-in-Salt electrolyte for high-energy rechargeable metallic lithium batteries, Nat. Commun. 4 (2013) 1–9. https://doi.org/10.1038/ncomms2513.

[45] Ruffo, R., Fathi, R., Kim, D.J., Jung, Y.H., Mari, C.M., Kim, D.K., Impedance analysis of $Na_{0.44}MnO_2$ positive electrode for reversible sodium batteries in organic electrolyte (2013) Electrochimica Acta, 108, pp. 575-582. DOI: 10.1016/j.electacta.2013.07.009

[46] F. Colombo, S. Bonizzoni, C. Ferrara, R. Simonutti, M. Mauri M. Falco, C. Gerbaldi, P. Mustarelli, R. Ruffo, Polymer-in-Ceramic Nanocomposite Solid Electrolyte for Lithium Metal Batteries Encompassing PEO-Grafted TiO2 Nanocrystals, J. Electrochem. Soc. 167 (2020) 070535.

[47] E. Simonetti, G. Maresca, G.B. Appetecchi; G.-T. Kim, N. Loeffler, S. Passerini, Towards Li(Ni0.33Mn0.33Co0.33)O2 /graphite batteries with ionic liquid-based electrolytes. I. Electrodes' behavior in lithium half-cells. J. Power Sources 331 (2016) 426-434.

[48] S. Brutti, E. Simonetti, M. De Francesco, A. Sarra, A. Paolone, O. Palumbo, S. Fantini, R. Lin,

A. Falgayrat, H. Choi, M. Kuenzel, S. Passerini, G.B. Appetecchi, Ionic liquid electrolytes for high-voltage, lithium-ion batteries. J. Power Sources 479 (2020) 228791.

Figures and Tables

*Table 1 – Sample labels and nominal composition expressed as molar ratio, weight ratio, molarity, and molality. *Na-sat composition: the nominal composition is 0.2:0.8 mole ratio, however a small amount of solid residue was observed. The actual composition was determined via NMR and Raman measurements (see text).*

Sample label	**NaTFSI (*x*)**	**$PYR_{13}TFSI$ (*x*)**	**NaTFSI (g)**	**$PYR_{13}TFSI$ (g)**	**m (mol kg^{-1})**	**wt.%**	**w:w**
IL-PT	0	1	0.0	100.0	0.000	0.000	0.0000
Na002	0.02	0.98	1.5	98.5	0.050	0.015	0.0153
Na005	0.05	0.95	3.8	96.2	0.130	0.038	0.0394
Na01	0.1	0.9	7.7	92.3	0.274	0.077	0.0832
Na-sat*	0.2	0.8	15.8	84.2	0.618	0.158	0.1872

Table 2 – Parameters obtained by VTF best-fit of the ionic conductivity data vs. reciprocal temperature reported in Figure 4. The parameter's meaning is explained in the text. T_g values are obtained from DSC data reported in Figure 1.

	IL-PT	Na002	Na005	Na01	Na-sat
σ_0 / S cm^{-1}	1.93	1.52	1.60	2.00	1.53
B /K^{-1}	574.1	487.6	531.4	661.2	525.4
T_0 /K	178	186	180	174	201
T_0 /°C	-95	-87	-93	-99	-72
T_g	-	-	-83	-80	-73

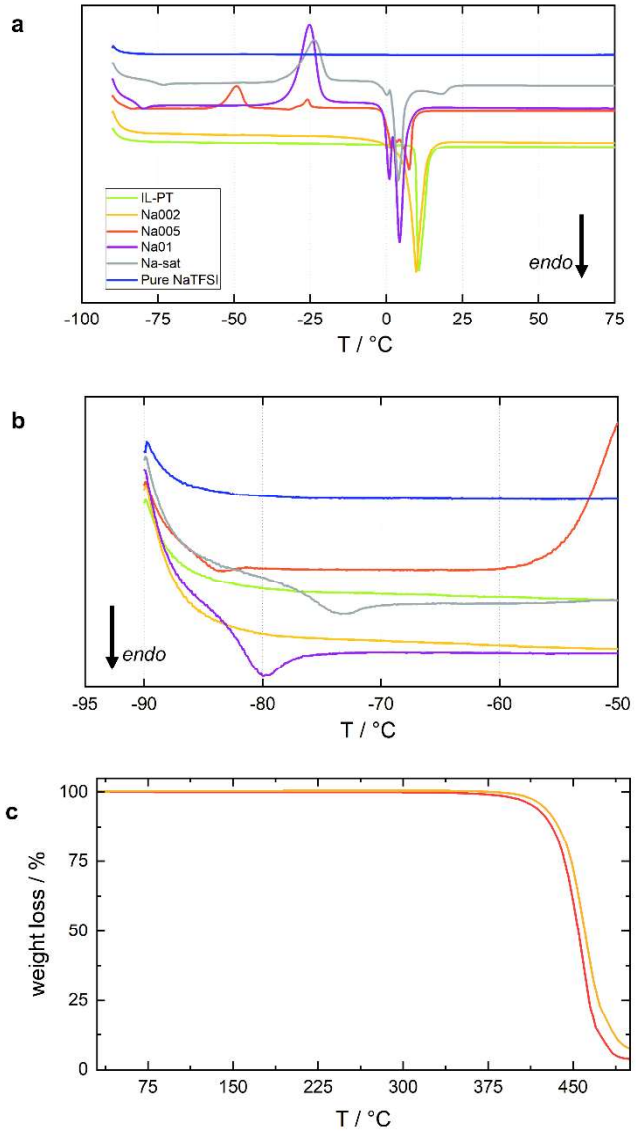

Figure 1 – DSC profiles for the Na002, Na005, Na01, Na-sat solutions and for the two end members - the pure IL and the pure NaTFSI salts - in the temperature ranges -95 °C; +75°C (a) and -95°C; -50 °C (b); TGA traces for th Na01 and Na-sat compositions (c).

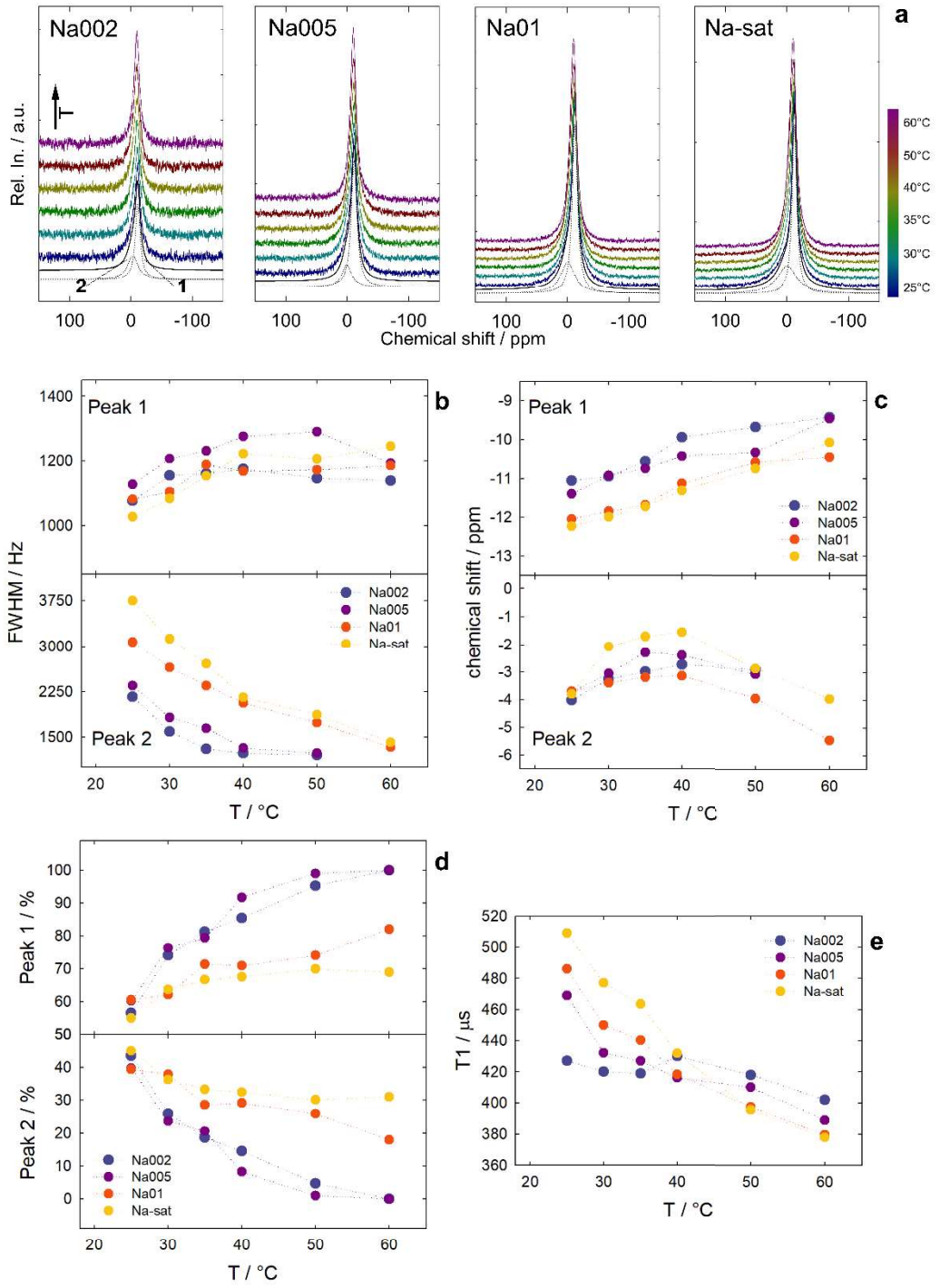

Figure 2 - ^{23}Na NMR spectra vs. temperature (25 °C, 30 °C, 35 °C, 40°C, 50°C, and 60 °C, increasing temperature from bottom to top) for the different compositions. For the spectra collected at 25 °C, the overall fit is presented (full lines) together with the two separated components (Peak 1 and Peak 2, dotted lines) (a); line broadening (Full Width at Half Maximum, FWHM) (b); chemical shift (c), relative intensity of the two components (d), and the global T_1 value (e).

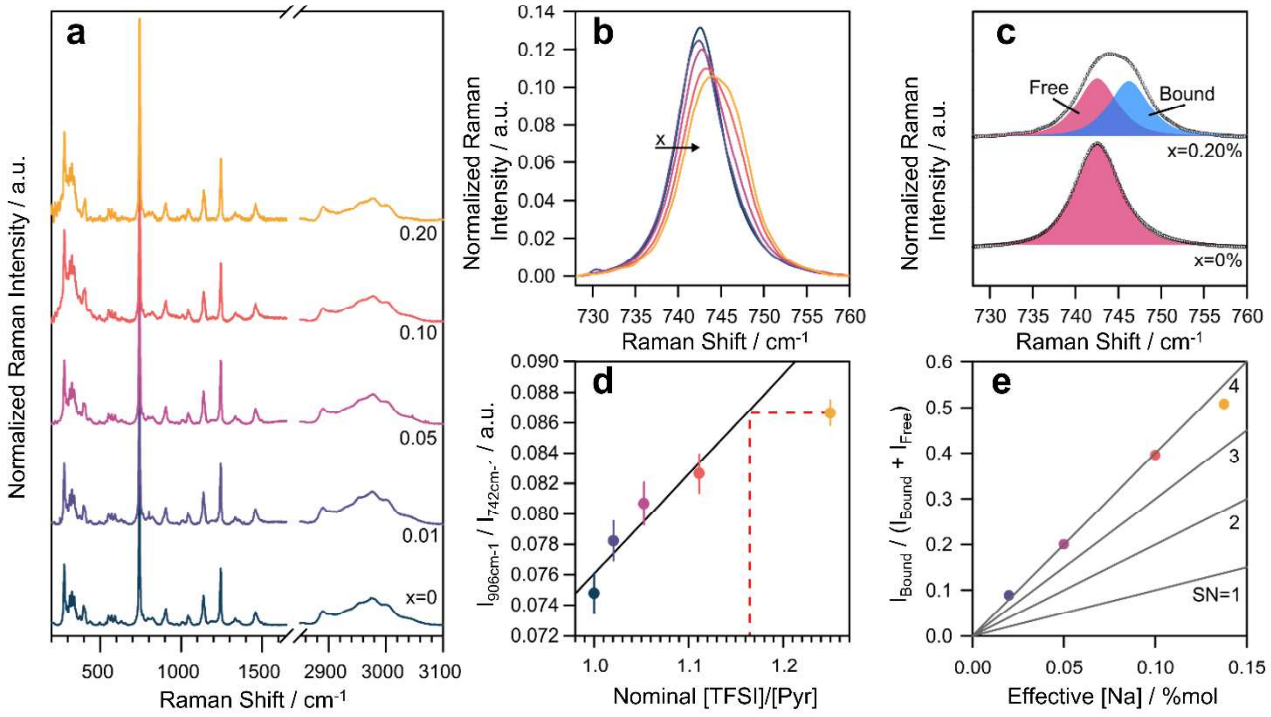

Figure 3 - Normalized Raman spectra of $Pyr_{13}TFSI$-NaTFSI (a). Raman spectra in the range 725-760 cm^{-1}, relative to the $TFSI^-$ -associated main bands, after integral normalization (b). Representative peak decomposition in free and bound moiety of $TFSI^-$ band for the $Pyr_{13}TFSI$ (IL-PT) and Na-sat samples (c). Analysis of the $TFSI^-$ /Pyr_{13}^+ bands ratio vs. the nominal ionic liquid molar concentration (d). Solvation number analysis extrapolated from the ratio of bound and free anion bands vs. the effective Na^+ concentration (e).

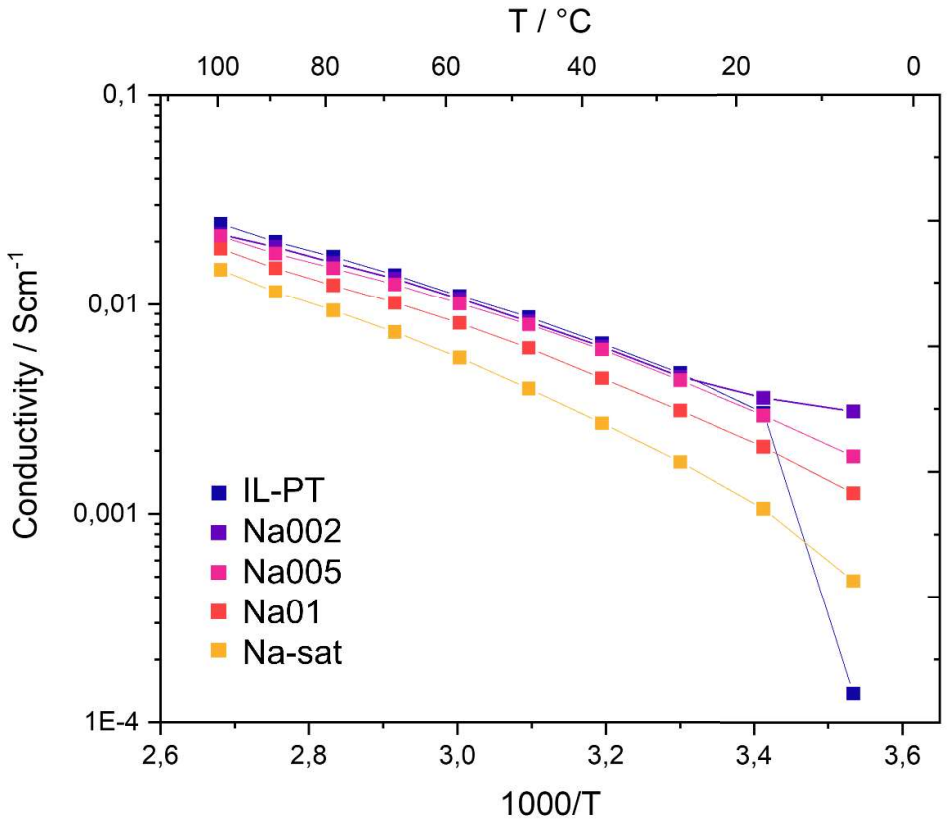

Figure 4 – Conductivity vs. temperature for all the samples.

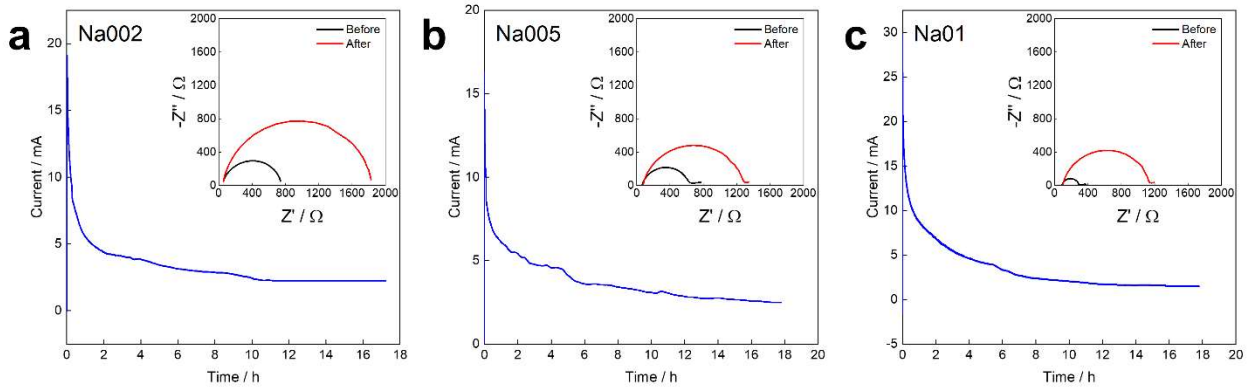

Figure 5: Chronoamperometry measurements of the Na|IL|Na cell used for the evaluation of the transference number for the Na002 (a), Na005 (b), and Na01 (c) samples. The impedance spectra are reported in the top-right part of the Figure.

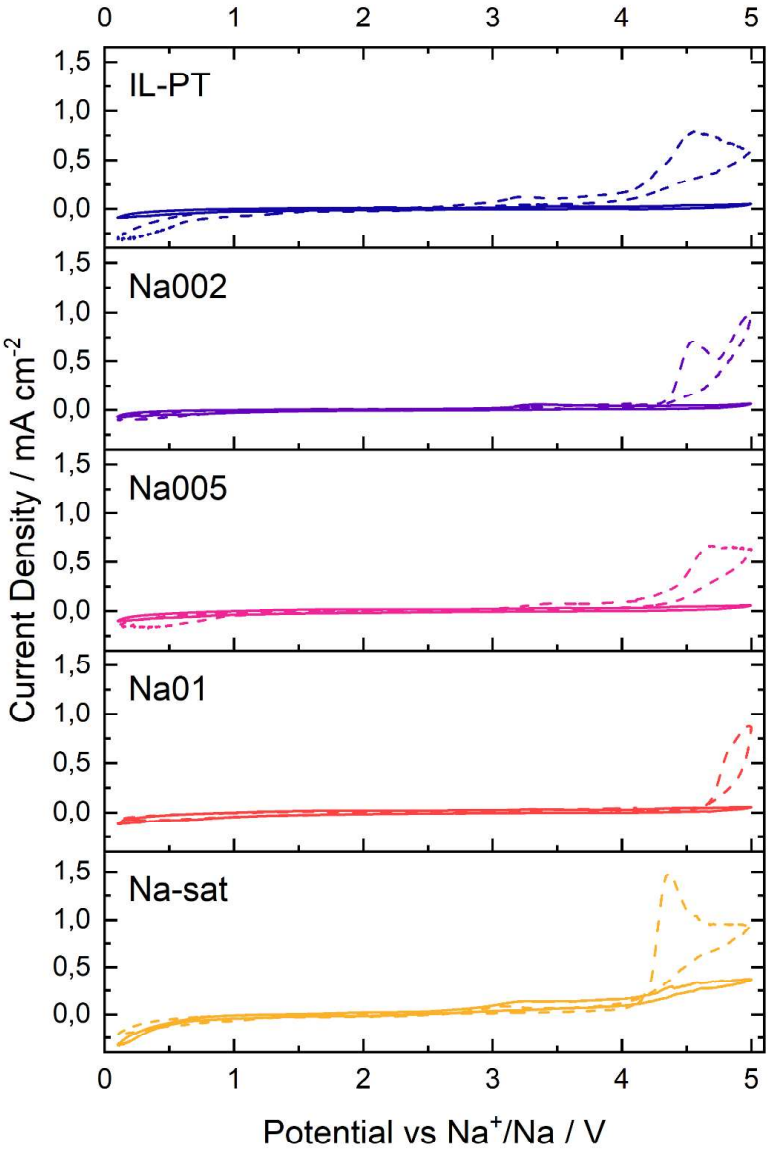

Figure 6: CV analyses of the different IL electrolytes tested in the potential range 0.1-5.0 V at fixed scan rate of 1.0 mv/s (1st and 5th cycles shown for each sample with dotted and continuous lines, respectively). All samples show high currents above 3V in the first cycle which reduces drastically with further cycling (formation of stable interphases).

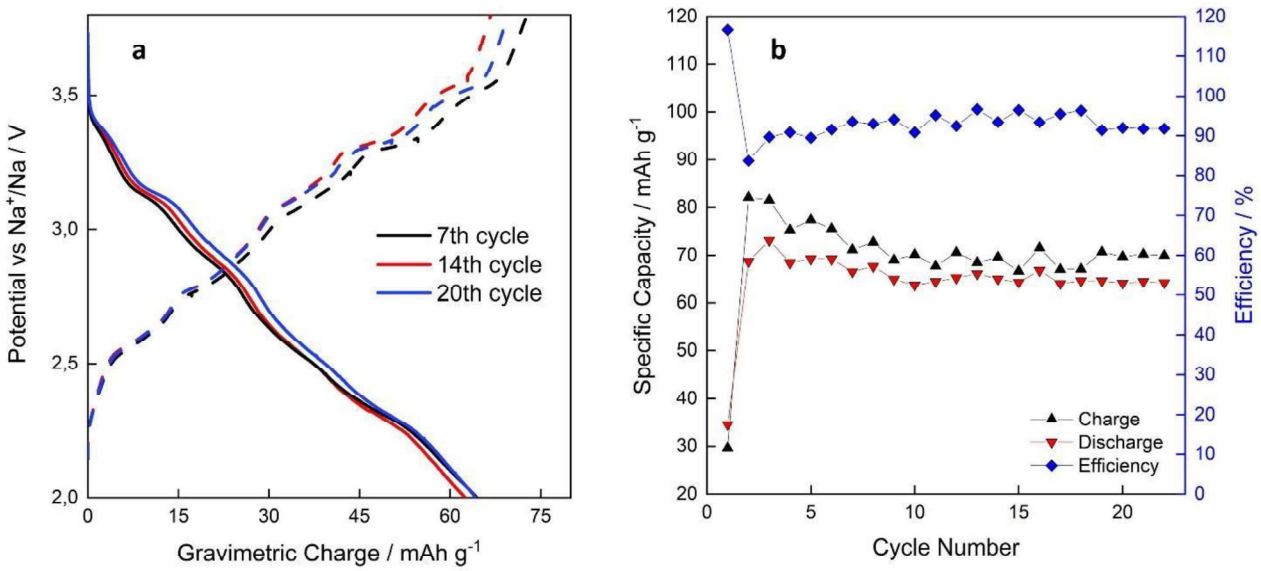

Figure 7: Charge-discharge profiles at selected cycles of a Na|IL|NMO cell employing Na01 sample and working at C/10 (a). Coulombic efficiency and charge/discharge capacity as a function of the number of cycles of the same cell (b).

Table of contents